

Ultrasensitive Mid-Infrared Biosensing in Aqueous Solutions with Graphene Plasmons

Chenchen Wu, Xiangdong Guo, Yu Duan, Wei Lyu, Hai Hu, Debo Hu, Ke Chen, Zhipei Sun, Teng Gao, Xiaoxia Yang,* and Qing Dai*

Identifying nanoscale biomolecules in aqueous solutions by Fourier transform infrared spectroscopy (FTIR) provides an in situ and noninvasive method for exploring the structure, reactions, and transport of biologically active molecules. However, this remains a challenge due to the strong and broad IR absorption of water which overwhelms the respective vibrational fingerprints of the biomolecules. In this work, a tunable IR transparent microfluidic system with graphene plasmons is exploited to identify ≈ 2 nm-thick proteins in physiological conditions. The acquired in situ tunability makes it possible to eliminate the IR absorption of water outside the graphene plasmonic hotspots by background subtraction. Most importantly, the ultrahigh confinement of graphene plasmons (confined to ≈ 15 nm) permits the implementation of nanoscale sensitivity. Then, the deuterium effects on monolayer proteins are characterized within an aqueous solution. The tunable graphene-plasmon-enhanced FTIR technology provides a novel platform for studying biological processes in an aqueous solution at the nanoscale.

nanomedicine targeting effects are at the nanoscale level.^[2] Thus, it is important to develop in situ and noninvasive methods with nanoscale resolutions to understand biological processes in physiological environments.^[3] Along these lines, Fourier transform infrared (FTIR) spectroscopy serves as a label-free, noninvasive, and fast method for identifying biomolecules by detecting their molecular vibrational fingerprints.^[4] However, achieving FTIR in aqueous solutions with nanoscale sensitivity remains a challenge since the strong and broad IR band of water (H_2O) always masks the vibrational fingerprints of the biomolecules, especially in the mid-IR range.^[5]

Many efforts have been made to implement the vibrational fingerprints masked by H_2O . For example, alternative solvents (e.g., D_2O , CCl_4 , and CS_2) are used in

FTIR measurements since their IR absorption bands are shifted away from the absorption band of H_2O .^[4] Another potential route is to shorten the effective IR optical path in an aqueous solution to suppress the interference of H_2O , such as the attenuated total reflectance (ATR).^[6] Nevertheless, neither solvent replacement nor ATR can enhance the FTIR sensitivity to the nanoscale due to the weak light–matter interaction. Therefore, the surface-enhanced infrared absorption (SEIRA) technique is developed for in situ probing nanoscale samples through the enhanced near-field of the surface plasmons.^[7] Although the metal-antenna-based SEIRA has already achieved high sensitivity, the detection limit is ultimately restricted to monolayer molecules by the relatively poor light confinement of metal in the mid-IR.

The extremely high light confinement of graphene plasmon renders it attractive for SEIRA applications.^[8] The sensitivity of graphene-plasmon-enhanced FTIR can reach sub-nanometer scale, which has been demonstrated in identifying molecules in the solid phase and the gas phase.^[8a,9] In addition, graphene can increase the IR absorption of molecules in aqueous solution in the inner reflection process,^[10] but the lack of tunability as well as the utilization of bulky ATR instrumentation prevents it from practical use.^[11]

In this work, we develop a tunable graphene-plasmon-enhanced FTIR technology to identify nanoscale proteins in physiological conditions. Specifically, the interference of H_2O outside the graphene plasmon hotspots is eliminated

1. Introduction

The length scale of a biomolecule is usually a few nanometers.^[1] For instance, protein is one of the most important nanoscale biomacromolecules, and the biomolecular corona interface, the host–pathogen recognition interactions as well as the

C. Wu, X. Guo, Y. Duan, W. Lyu, H. Hu, D. Hu, K. Chen, T. Gao, X. Yang, Q. Dai


CAS Key Laboratory of Nanophotonic Materials and Devices
CAS Key Laboratory of Standardization and Measurement for Nanotechnology

CAS Center for Excellence in Nanoscience
National Center for Nanoscience and Technology
Beijing 100190, China

E-mail: yangxx@nanoctr.cn; daiq@nanoctr.cn

C. Wu, X. Guo, H. Hu, D. Hu, K. Chen, X. Yang, Q. Dai
Center of Materials Science and Optoelectronics Engineering
University of Chinese Academy of Sciences
Beijing 100049, China

Z. Sun
Department of Electronics and Nanoengineering and QTF Centre of Excellence
Department of Applied Physics
Aalto University
Espoo 02150, Finland

 The ORCID identification number(s) for the author(s) of this article can be found under <https://doi.org/10.1002/adma.202110525>.

DOI: 10.1002/adma.202110525

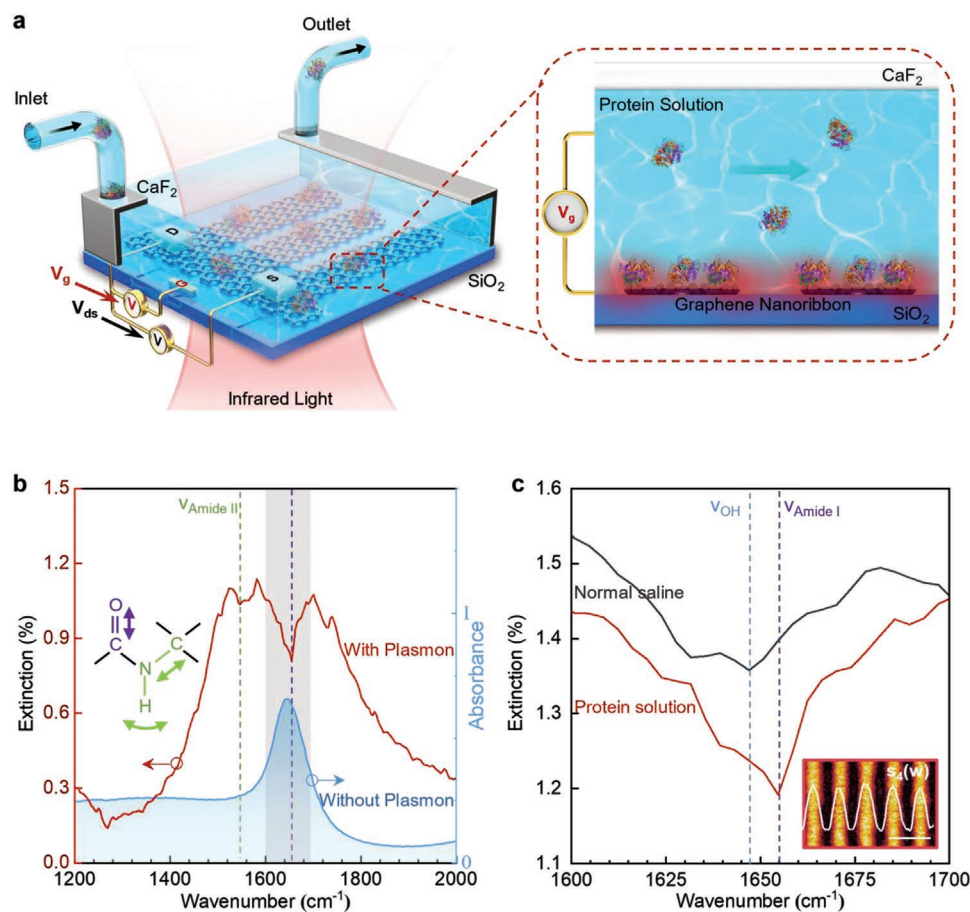


Figure 1. Tunable graphene-plasmon-enhanced FTIR platform. a) Schematic diagram of the GP-aIR biosensor. The graphene plasmonic devices are integrated in an IR transparent microfluidic system, whereas a 200 μm -thick calcium fluoride (CaF_2) crystal is chosen as the top window. Graphene plasmons are excited using incident IR light and tuned in situ by gating. The plasmon resonances are coupled with proteins in the hotspots. b) FTIR spectra of protein solution (5 mg mL^{-1}) in the microfluidic system with/without graphene plasmon enhancement. c) The magnified mid-IR region (1600–1700 cm^{-1}) for graphene-plasmon-enhanced FTIR before (gray curve) and after (red curve) protein adsorption in aqueous solution. $E_f = 0.3$ eV, graphene nanoribbon width is ≈ 60 nm, and the period is ≈ 120 nm. Inset: Near-field optical image of graphene nanoribbon at an IR wavelength of 10.526 μm (i.e., 950 cm^{-1}), scale bar: 200 nm.

via performing an in situ background subtraction method by gating in the FTIR measurement. Most importantly, the ultra-high confinement of graphene plasmons (confined to ≈ 15 nm) permits the implementation of nanoscale sensitivity (down to ≈ 2 nm-thick proteins). The superior sensitivity in the physiological environment enabled by our approach, in turn, allows the direct monitoring of the protein hydrogen(H)/deuterium(D) exchange process within an aqueous solution by performing FTIR transmission measurements.

2. The Tunable Graphene-Plasmon-Enhanced FTIR in Aqueous Solutions

The proposed tunable graphene plasmonic aqueous IR (GP-aIR) biosensor is schematically illustrated in **Figure 1a**. As shown, it consists of graphene plasmonic devices and an IR transparent microfluidic system (see details in the Experimental Section and Figure S1 in Supporting Information). It is underlined that the high IR transmittance is the foundation

for the implementation of graphene-plasmon-enhanced FTIR measurements. To achieve high IR transparency in aqueous FTIR measurements, a 200 μm -thick calcium fluoride (CaF_2) crystal is chosen as the top window, whereas a SiO_2 /high-resistivity Si substrate supports the graphene plasmonic devices as the bottom window of the microfluidic chamber. More importantly, the height of the microfluidic chamber at the graphene nanoribbon region (100 $\mu\text{m} \times 200 \mu\text{m}$) is designed to be less than 5 μm for ensuring the steady flowing of the solution, as well as a high IR transparency for the FTIR measurements. As a result, the IR absorbance of this microfluidic chamber in the graphene nanoribbon region is less than 0.6 after filling with a protein solution (the blue curve in Figure 1b). We want to state that although CaF_2 crystal (working as a transparent top window and replaceable) is slightly dissolvable in water, it is found that the GP-aIR biosensor shows high stability and consistent plasmonic response in water for more than 48 hours.

To excite mid-IR plasmons, the graphene on the substrate is patterned to nanoribbon arrays with widths between 50 and 100 nm by the electron beam lithography and the oxygen

plasma etching (details in the Experimental Section and Figure S2 in Supporting Information). A pair of gold electrodes with a titanium adhesion layer is evaporated on the graphene as the source and drain contacts, whereas another electrode is evaporated outside the graphene to play the role of the gate contact. An electric double layer (EDL) formed on the graphene and the gold electrodes in the protein solution works as a dielectric layer for the modulation of the graphene Fermi level by gating. A 200 nm-thick poly(methyl methacrylate) film as the passivation layer is coated on the source and drain electrodes for preventing the direct interaction of the electrode materials with the aqueous solution and minimizing the current leakage. The extinction spectra are obtained by in situ modulating the gate voltage, i.e., $1 - T_{E_F}/T_0$, where T_{E_F} is the transmittance measured at a specific graphene Fermi level (E_F), whereas T_0 is measured at the graphene charge neutral point (CNP, where there is no graphene plasmon excited). Thus, the background signal outside the plasmonic hotspot region is eliminated, and only the plasmon-related signals are detected.

The red curve in Figure 1b depicts a typical extinction spectrum as measured with 5 mg mL⁻¹ protein solution after flowing for 1 h. It is interesting to notice that two sharp dips at 1545 cm⁻¹ (marked with a green line) and 1655 cm⁻¹ (marked with a purple line) on the broad graphene plasmonic resonance peak can be detected. This comes from the destructive interference of the graphene plasmon and the molecular vibrations. Therefore, the recorded dip at 1545 cm⁻¹ can be identified as the amide II band, which is a typical protein molecular signature. However, the dip at 1655 cm⁻¹ is at a region overlapped by the OH-bending mode of the water and the amide I band of the protein. To shed light on these outcomes, the region between the wavenumber from 1600 to 1700 cm⁻¹ is magnified and is compared with the extinction spectrum of graphene plasmon in the normal saline (as is divulged in Figure 1c). The extinction spectrum of graphene plasmon in the normal saline exhibits the water OH-bending mode at around 1645 cm⁻¹ (the gray

curve in Figure 1c), while there is about 10 cm⁻¹ shift of the peak to the 1655 cm⁻¹ for the protein solution which is more close to the amide I band of the protein (more details can be found in Figure S3, Supporting Information). Thus, the signal strength of the protein exceeds that of water in the extinction spectrum, implying the existence of more protein molecules than water molecules in the plasmon hotspots on the graphene nanoribbons.

We perform theoretical calculations to repeat the measured extinction spectra (see details in Figure S4 and Note S1 in the Supporting Information), and find that the density of the proteins is enriched by $\approx 3 \times 10^4$ times on the graphene nanoribbons compared with that of the protein solution. This result implies the protein adsorption on the graphene surface. Considering our previous works, the physisorption of molecules on graphene is regarded as the driving force.^[9d,12] More importantly, a hydrophobic-based graphene surface is more likely to adsorb the proteins with hydrophobic groups.^[13] The enriched proteins on graphene nanoribbons are schematically revealed on the right of Figure 1a. We want to underline that the electromagnetic field distribution is confined around the graphene nanoribbons due to the manifestation of the plasmonic resonances (illustrated as the inset shown in Figure 1c). Therefore, as the proteins are adsorbed on the nanoribbons, their IR absorptions are enhanced dramatically by the graphene plasmon. Thus, our tunable graphene-plasmon-enhanced FTIR platform discloses superior sensitivity for the identification of proteins even in an aqueous solution.

Additionally, the liquid gate via EDL permits the modulation of the graphene plasmons in a wide frequency range. A typical transfer characteristic curve of the GP-aIR biosensor after the physisorption-based saturation of the proteins in the aqueous solution is highlighted in Figure 2a (blue line). The graphene E_F can be calculated by applying a parallel plate capacitor model. The sub-nanometer thin EDL is formed on both the graphene and gold electrodes in the protein solution, which operates via

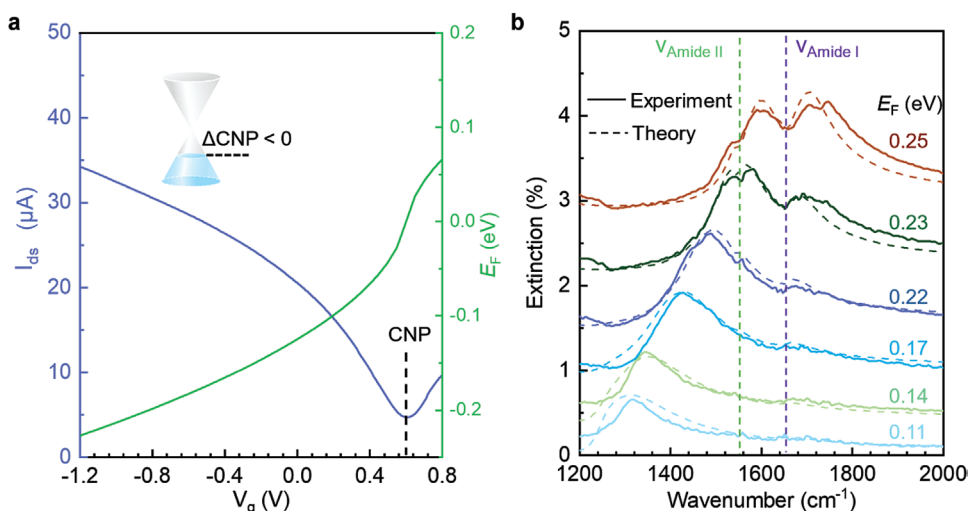


Figure 2. Selective probing of proteins with electrically tunable graphene plasmons. a) Transfer characteristic curve and the corresponding E_F of the graphene plasmonic device. b) The solid curves are experimental results of the graphene plasmon response at different gate voltages; the dashed curves are simulation results of the same graphene nanoribbon at different E_F . The experimental results are collected after 1 mg mL⁻¹ protein solution flowing for 2 h, the graphene nanoribbon width is ≈ 50 nm, and the period is ≈ 100 nm.

a liquid gate and has a higher modulation efficiency than the back-gate with the SiO₂ dielectric layer.^[14] The estimated liquid-gate capacitance of our GP-aIR biosensor in the protein solution is $C_{\text{top}} \approx 385 \text{ nF cm}^{-2}$, whereas the corresponding E_F is depicted by the green curve in Figure 2a (see Note S2 in the Supporting Information).

The extinction spectra of the GP-aIR biosensor at different E_F are shown in Figure 2b. As shown, the plasmon resonance frequency is dynamically modulated from the value of ≈ 1300 to 1700 cm^{-1} when E_F is adjusted from ≈ 0.11 to 0.25 eV . More importantly, the coupling strength of the protein vibrational mode is enhanced as the detuning of the graphene plasmons and the molecular vibrational modes decrease, which is consistent with the acquired numerical calculation results (the dashed curves in Figure 2b). When the plasmon resonance frequency is shifted from about 1300 to 1560 cm^{-1} , the dip at 1545 cm^{-1} gets deeper, implying that the coupling strength between the graphene plasmon and the amide II band is enhanced. With a further increase of E_F to 0.25 eV , this dip at 1545 cm^{-1} becomes shallower, whereas the dip at 1655 cm^{-1} gradually deepens due to the stronger coupling between the amide I band and graphene plasmons. The coupling mechanism between graphene plasmons and molecular vibrational modes can be described as a coupling process between two harmonic oscillators. The excitation of molecular vibration by far-field incident IR light can be ignored compared to that by the graphene plasmon due to the significant size mismatch between the molecules and the IR light wavelength.^[8b,15] Therefore, it is possible to tune the graphene Fermi energy and realize selective plasmonic response in the mid-IR to identify protein vibrational fingerprints by enforcing different gate voltages.

3. Protein Identification with Ultrahigh Sensitivity

Here, we investigate the detection limit of the proposed GP-aIR biosensor by monitoring the adsorption process of protein on the graphene nanoribbons. When protein solution is injected into the GP-aIR biosensor, the proteins are gradually adsorbed on the graphene nanoribbons and finally reach a saturated state in 20 min. The extinction spectra of the GP-aIR biosensor, which are measured at different times during this process, are disclosed in Figure S5 in the Supporting Information. To exhibit the plasmon-enhanced molecular signals more clearly, we extract them from the plasmon resonance peaks in the as-measured extinction spectra, as demonstrated in Figure 3a. At the beginning of injecting the protein solution (0 min), only one broad peak at around 1645 cm^{-1} can be recorded due to the OH-bending mode of the water. As the adsorption time becomes longer (injecting the protein solution for 7, 8, 16, 20 min), the acquired IR response of the amide II band ($\approx 1545 \text{ cm}^{-1}$) appears and constantly enhances as indicated by a green arrow. The IR response near 1645 cm^{-1} is blueshifting to 1655 cm^{-1} , which can be identified as the amide I band of protein (purple arrow).

To further understand the adsorption process, we perform simulations based on the finite-element method (see details in the Experimental Section). The obtained extinction spectra are in excellent agreement with the respective experimental spectra

when considering the adsorbed protein layer with the following thickness values: 0, 2, 4, 6, and 8 nm (Figure 3c). We have also to underline that the thicknesses of the protein layers are consistent with the experimentally measured values. On top of that, we carried out atomic force microscopy (AFM) measurements on the graphene nanoribbons at different adsorption times. The GP-aIR biosensor taken out of the protein solution is washed with deionized water several times and dried in flowing nitrogen. As can be observed from Figure 3b and Figure S6 in the Supporting Information, the height of the graphene nanoribbons increases from ≈ 2 to $\approx 8 \text{ nm}$ with increasing adsorption time, which verifies that proteins are gradually adsorbed on the graphene nanoribbons.

The acquired electrical response can also support the measured results of the proposed GP-aIR biosensor. The proteins are negatively charged in our protein solution since its pH value (about 7) is larger than the isoelectric point of the bovine serum albumin (BSA) protein (5.3).^[14a] Thus, there are electrons transferred to the graphene film after the protein adsorption. To exclude the n-doping effect of other ions in the protein solution,^[16] normal saline is first injected inside until the CNP of the GP-aIR biosensor stabilizes, and then the protein solution with the same NaCl concentration as normal saline is injected. The transfer characteristics of the GP-aIR biosensor are measured at different times during the protein adsorption process to calculate the induced change of the CNP value (the inset in Figure 3d). As demonstrated in Figure 3d, the protein adsorption shifts the graphene Fermi level toward the Dirac point. It changes fast at the beginning, and then the speed of the change becomes slow and finally reaches saturated adsorption ($\Delta E_F \approx 90 \text{ meV}$). The change law and the time required for the saturated adsorption displayed by the electrical results corroborated the extinction spectra of the GP-aIR biosensor.

These results point out that the GP-aIR biosensor is sensitive to the presence of proteins in an aqueous solution due to the high sensitivity of the graphene plasmons (obvious response for 2 nm protein), as well as to the adsorption of molecules on graphene. In addition, protein solutions with different concentrations are measured, and the outcomes of 100 pg mL^{-1} and 100 ng mL^{-1} solutions are revealed in Figure S7 in the Supporting Information. After adsorbing proteins in the solution for 2 h, both the amide I and amide II bands can be identified by the GP-aIR biosensor.

4. Monitoring the H/D Exchange Process of Proteins

H/D exchange is widely used in exploring protein structures and functions for identifying and understanding the complex biological processes and developing pharmaceutical drugs.^[17] The exposure of proteins to D₂O induces H/D exchange in disordered regions that lack stable hydrogen bonding. It is stated that the tightly folded elements are much more protected from the H/D exchange resulting thus in slow isotope exchange.^[18] The investigation of the interaction rate and sites of the H/D exchange process between the hydrogens of the protein backbone and its surrounding solvent reflects not only the folded state of the protein and its dynamics but also the

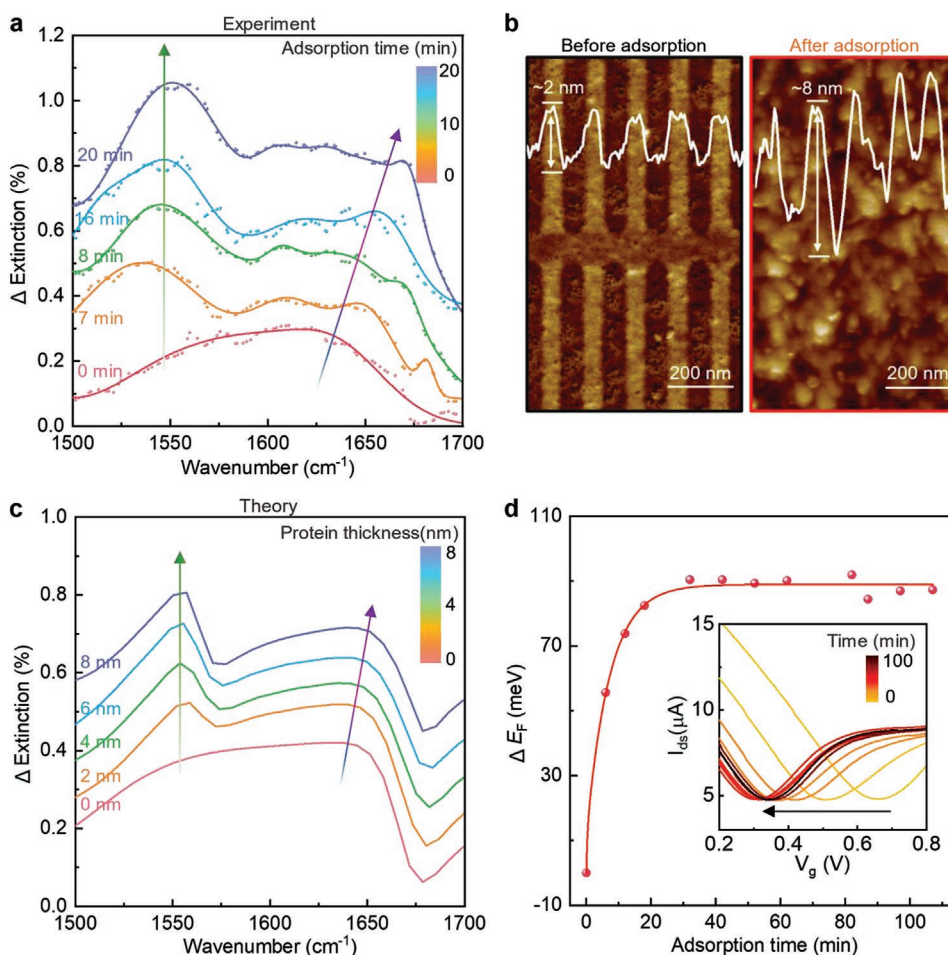


Figure 3. Identification of proteins during the adsorption process in physiological conditions. a) Plasmon-enhanced protein IR responses (Δ Extinction) at different adsorption times (0, 7, 8, 16, 20 min). The graphene nanoribbon width is ≈ 70 nm, the period is ≈ 140 nm, and the protein solution concentration is 5 mg mL^{-1} . b) Morphologies and respective AFM height data of the graphene nanoribbons before and after 1 h of protein adsorption. c) Simulated Δ Extinction of graphene-plasmon-enhanced protein IR response with different adsorption thicknesses (0, 2, 4, 6, 8 nm). The parameters of the graphene device are the same as those in (a), and the E_F is set as 0.25 eV. d) The E_F of the GP-aIR biosensor changes during the protein adsorption process, extracted from the transfer characteristic curves as shown in the inset.

intrinsic chemical properties of the underlying amino acid sequence.^[17b] NMR spectroscopy is currently the most important method to characterize proteins in solution by analyzing the NMR signal of the nuclei of atoms in the protein, but it relies on expensive and complicated equipment and strict sample preparation. A fast and noninvasive method to directly monitor the proton exchange process in an aqueous solution is still missing.

Along these lines, we demonstrate that the tunable graphene-plasmon-enhanced FTIR platform can directly monitor the H/D exchange of nanoscale proteins within the aqueous solution. Initially, the GP-aIR biosensor is flowing with a protein solution (solvent: H_2O) for 1 h for reaching saturated adsorption of the proteins on the graphene nanoribbons. Subsequently, D_2O is injected into the microfluidic system for half an hour to make sure a complete H/D exchange for the proteins. Then, H_2O and D_2O are alternately injected several times, and the extinction spectra of graphene plasmon are measured simultaneously (see Figure S8c, Supporting

Information). For comparison, the plasmon-enhanced protein responses are extracted and disclosed in Figure 4a. The most obvious change in the acquired spectra is that the peak at 1545 cm^{-1} corresponding to the amide II band disappears and a new peak appears at 1457 cm^{-1} by replacing the H_2O with D_2O , and they recover when reinjecting H_2O . This provides direct evidence for the H/D exchange. According to the literature, the peak at 1457 cm^{-1} is assigned to the amide II band of deuterated protein, arising from the coupling of the N–H/D bending and C–N stretching modes (Figure 4b).^[19] However, the peak intensity at 1457 cm^{-1} is much larger than that at 1545 cm^{-1} , which may be related to the H–O–D in D_2O (with bending modes at 1457 cm^{-1}). Due to the hygroscopicity of D_2O , there is also a small amount of H_2O in our D_2O , as manifested by the IR spectrum (see Figure S8a, Supporting Information). Additionally, during this H/D exchange process, the amide I band (C=O stretching) of protein at 1655 cm^{-1} has a slight redshift because the effect of hydrogen bonds on the secondary structure is slightly different in different solvents.

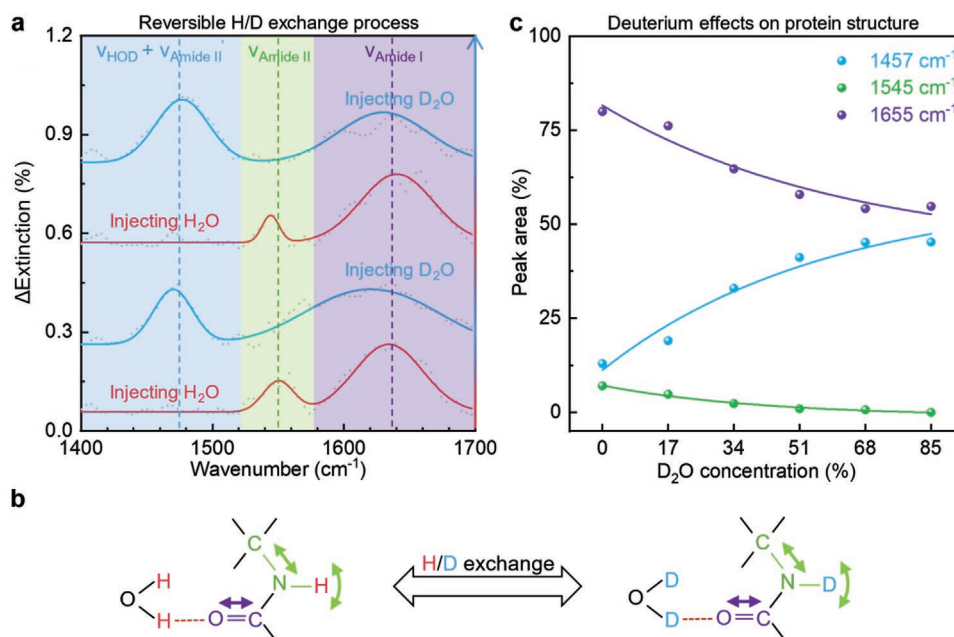


Figure 4. H/D exchange processes monitored by the GP-aIR biosensor. a) In situ and real-time identification of proteins in H_2O and D_2O which are alternately injected several times. The protein concentration is 1 mg mL^{-1} . The plasmon-enhanced protein responses (Δ Extinction) are extracted from Figure S8c in the Supporting Information. b) Illustration of $\text{D}_2\text{O}/\text{H}_2\text{O}$ -induced molecular structure change and hydrogen bond interaction. c) The plasmon-enhanced peak area of ≈ 1457 , ≈ 1545 , and $\approx 1655 \text{ cm}^{-1}$ is extracted from graphene-plasmon-enhanced FTIR at different D_2O concentrations (17%, 34%, 51%, 68%, 85%) in Figure S8d in the Supporting Information.

Furthermore, the effects of H/D exchange process on the protein molecular structures is investigated by varying the ratio of D_2O and H_2O in the solution. The extinction spectra at each D_2O concentration are collected (see Figure S8d, Supporting Information), while the plasmonic enhanced signals are extracted and plotted in Figure 4c. Compared with the extinction spectrum in H_2O , the intensities of both the amide I band (around 1655 cm^{-1}) and the amide II band (around 1545 cm^{-1}) decrease by increasing the concentration of D_2O . On top of that, the ratio of H/D exchange is consistent with the ratio of $\text{H}_2\text{O}/\text{D}_2\text{O}$, indicating that the H/D exchange process of nanoscale proteins occurs with high efficiency and reaches a dynamic equilibrium. The reason is that nanoscale proteins have a large proportion of surface structures exposed to the environment. From this outcome, we can conclude that our approach exhibits high detection sensitivity and can monitor the proton exchange process of nanoscale-based proteins.

5. Conclusion

We have identified nanoscale protein fingerprints in physiological conditions by employing a tunable graphene-plasmon-enhanced FTIR platform. The highly confined optical field and tunability of the graphene plasmons can essentially enhance the light-matter interaction and recede the water interference, which pushes the sensitivity down to $\approx 2 \text{ nm}$ -thick proteins. Meanwhile, we exhibit the dynamic and reversible H/D exchange on the protein molecular structure with the assistance of the GP-aIR biosensor. Interestingly, D_2O is found to affect the nanoscale protein structures by hydrogen bonds effects

on secondary structure and N-H/N-D exchange on the amide II band. The exciting performance of our approach paves the way for the implementation of an in situ studying bioprocesses within complex physiological conditions with ultrahigh sensitivity, which provides a new strategy for studying the nano-bio interface and opens an inspiring outlook for both nanotoxicology and nanopharmacology.

6. Experimental Section

Graphene Plasmonic IR Biosensing in Aqueous Solutions: The proposed graphene plasmonic devices were composed of connected graphene nanoribbon arrays patterned on a SiO_2/Si substrate (N/Phos doped, $1\text{--}10 \ \Omega \text{ cm}$, from Silicon Valley Microelectronics, Inc.) and were encapsulated within the microfluidic system by utilizing O rings made of nitrile butadiene. The graphene layer was grown on copper foil by chemical vapor deposition method and consequently transferred to a $285 \text{ nm SiO}_2/500 \ \mu\text{m Si}$ substrate using the wet transfer method. The graphene film was in high quality, as confirmed by the optical image (see Figure S2a, Supporting Information), the scanning electron microscopy image (see Figure S2b, Supporting Information), and the Raman spectra (see Figure S2c, Supporting Information). The carrier mobility of the graphene was $\approx 900 \text{ cm}^2 \text{ V}^{-1} \text{ s}^{-1}$, which was extracted from the transfer characteristic curve of the GP-aIR biosensor. Next, the nanoribbon arrays were patterned in graphene by using electron-beam lithography (Vistec 5000+ES, Germany) and then etched with oxygen plasma (SENTECH, Germany). The electrodes (5 nm Ti and 50 nm Au) were patterned and evaporated using electron-beam lithography combined with electron beam evaporation (OHMIKER-50B, Taiwan). Moreover, the in situ IR microfluidic system was custom-made by Zeptools Co. The thickness of the microfluidic chamber at the graphene nanoribbon region ($100 \ \mu\text{m} \times 200 \ \mu\text{m}$) was designed to be less than $5 \ \mu\text{m}$ controlled by a gold spacer. In comparison, the thickness of the remaining region was $200 \ \mu\text{m}$ which

was fabricated by photolithography (SUSS Ma-6, Germany) and deep reactive ion etching (Oxford Plasmalab System 100 ICP 180, UK).

Characterization of the Graphene Plasmon Devices: The morphologies and thicknesses of the fabricated graphene nanoribbons were characterized by employing scanning electron microscopy (NOVA Nano SEM 430) and AFM (Bruker ICON2-SYS) measurements. As far as the quality of the graphene and defect density of the nanoribbons were concerned, they were measured by Raman spectroscopy (Horiba Jobin Yvon LabRAM HR800) with laser excitation at 514 nm, the laser power was 10%, and laser beam spot was $\approx 1 \mu\text{m}$. The electrical properties were determined by using a source meter (Keithley 2636B). In addition, FTIR transmission measurements were performed with Thermo Fisher Nicolet iN10 with an IR microscope (15 \times objective). The aperture was set as 100 $\mu\text{m} \times 200 \mu\text{m}$ for each measurement, while the resolution was 8 cm^{-1} and scans were 128. The volume required to fill the microfluidic system and permit the steady flow was $\approx 0.1 \text{ mL}$, measured by filling with a syringe pump. The chamber was filled with a protein solution for static measurements, whereas the inlet and outlets were sealed to prevent flow. During the flowing measurements, a constant flow rate of 0.0083 mL min^{-1} was maintained. The Keithley 2636B source-meter was also employed to tune the top gate voltage.

Near-Field Optical Microscopy Measurements: Near-field imaging was conducted by using a commercially available s-SNOM (Neaspec GmbH), equipped with IR lasers (890–1700 cm^{-1}). The P-polarized IR light from the monochromatic quantum cascade lasers was focused via a parabolic mirror onto both the tip and sample at an angle of 60 $^\circ$ to the surface normal. The probes were made initially for metalized AFM with an apex radius of $\approx 20 \text{ nm}$ (Nanoworld).

Electromagnetic Simulations and Theory: The electromagnetic simulations are conducted by using the commercial field solver, COMSOL Multiphysics. The graphene optical response is described via the Drude model. The employed protein solution parameters, including oscillator strength to each FTIR peak, are extracted, and fit the BSA film's measured IR absorbance. The simulation results are calculated by constructing a model utilizing a finite element electromagnetic simulation method. The graphene nanoribbon is modeled as a material with finite thickness and an equivalent relative permittivity distribution that depended on the thickness. The equal relative permittivity ϵ_g is derived from the surface conductivity σ of the graphene, calculated by the following expression: $\epsilon_g = 1 + i\sigma/\epsilon_0\omega t_g$, where ϵ_0 is the permittivity of the free space, ω is the angular frequency of the incident light, and t_g is the graphene layer thickness. The graphene is modeled as a thin film and treated as the transition boundary condition with a thickness of just 0.34 nm. At room temperature ($T = 300 \text{ K}$), the graphene surface conductivity could be approximately calculated from the Drude model^[20]

$$\sigma = \frac{ie^2 E_F}{\pi \hbar^2 (\omega + i/\tau)} \quad (1)$$

where e is the electron charge, \hbar is the reduced Planck constant, and E_F is the Fermi energy of graphene. The relaxation time is $\tau = \mu E_F / e v_F$, where $v_F = 1 \times 10^6 \text{ m s}^{-1}$ is the Fermi velocity, and $\mu \approx 900 \text{ cm}^2 \text{ V}^{-1} \text{ s}^{-1}$ is the carrier mobility extracted from experimental results.

The protein permittivity is retrieved from the experimental results by adjusting a Lorentzian permittivity^[7c,8a]

$$\epsilon_{\text{protein}} = \epsilon_\infty + \sum_{j=1}^2 \frac{S_j^2}{\omega_j^2 - \omega^2 - \Gamma_j \omega} \quad (2)$$

The extracted protein permittivity parameters from the experimental protein IR spectrum were: $\epsilon_\infty = 2.08$, $\omega_1 = 1655 \text{ cm}^{-1}$, $\omega_2 = 1545 \text{ cm}^{-1}$, $S_1 = 213 \text{ cm}^{-1}$, $S_2 = 124 \text{ cm}^{-1}$, $\Gamma_1 = 55.6 \text{ cm}^{-1}$, $\Gamma_2 = 62 \text{ cm}^{-1}$. The simulation outcomes are in good agreement with the experimental absorption data. In the protein solution, the water IR absorption signal is much stronger than the proteins. Assuming that proteins are adsorbed on the graphene surface and considering the field contribution of the graphene plasmons, a protein layer with a thickness of 8 nm and a water layer

with a thickness of 50 nm is utilized in the model for simplifying the calculation.

The Chemicals Sampling: The normal saline was 0.9% NaCl solution was prepared by dissolving NaCl (purity larger than 99.5%) in deionized water with a 100 mL volumetric flask. Moreover, the protein solution was prepared by dissolving BSA (from KEH, Biotechnology Grade) in normal saline. D₂O was purchased from Macklin with 99.9 at% D.

Supporting Information

Supporting Information is available from the Wiley Online Library or from the author.

Acknowledgements

This work was supported by the National Key R&D Program of China (2021YFA1201500), the National Natural Science Foundation of China (51925203, 52022025, 52102160, 51972074, 11974023, 52021006, and U2032206), the Strategic Priority Research Program of the Chinese Academy of Sciences (XDB30000000 and XDB36000000), Youth Innovation Promotion Association C.A.S., C.A.S. Interdisciplinary Innovation Team (JCTD-2018-03), the '2011 Program' from the Peking-Tsinghua-IOP Collaborative Innovation Center of Quantum Matter, the Open Project of Nanjing University (M34034), the Academy of Finland (314810, 333982, 336144, and 336818), the Academy of Finland Flagship Programme (320167,PREIN), the European Union's Horizon 2020 research and innovation program (820423,S2QUIP; 965124, FEMTOCHIP), the EU H2020-MSCA-RISE-872049 (IPN-Bio), The Business Finland (ALDEL), and ERC (834742).

Conflict of Interest

The authors declare no conflict of interest.

Data Availability Statement

The data that support the findings of this study are available from the corresponding author upon reasonable request.

Keywords

aqueous solutions, biosensing, graphene plasmons, surface-enhanced infrared spectroscopy

Received: December 25, 2021

Revised: April 18, 2022

Published online: May 29, 2022

- [1] K. A. Dawson, Y. Yan, *Nat. Nanotechnol.* **2021**, *16*, 229.
- [2] a) M. P. Monopoli, C. Åberg, A. Salvati, K. A. Dawson, *Nat. Nanotechnol.* **2012**, *7*, 779; b) S. Schöttler, G. Becker, S. Winzen, T. Steinbach, K. Mohr, K. Landfester, V. Mailänder, F. R. Wurm, *Nat. Nanotechnol.* **2016**, *11*, 372; c) P. M. Kelly, C. Åberg, E. Polo, A. O'Connell, J. Cookman, J. Fallon, Ž. Krpetić, K. A. Dawson, *Nat. Nanotechnol.* **2015**, *10*, 472.
- [3] a) B. S. Gomes, B. Simões, P. M. Mendes, *Nat. Rev. Chem.* **2018**, *2*, 0120; b) S. Tenzer, D. Docter, J. Kuharev, A. Musyanovych, V. Fetz, R. Hecht, F. Schlenk, D. Fischer, K. Kiouptsi, C. Reinhardt,

- K. Landfester, H. Schild, M. Maskos, S. K. Knauer, R. H. Stauber, *Nat. Nanotechnol.* **2013**, *8*, 772; c) F. Chen, G. Wang, J. I. Griffin, B. Brenneman, N. K. Banda, V. M. Holers, D. S. Backos, L. Wu, S. M. Moghimi, D. Simberg, *Nat. Nanotechnol.* **2017**, *12*, 387.
- [4] B. H. Stuart, *Infrared Spectroscopy: Fundamentals and Applications*, John Wiley & Sons, New York **2004**.
- [5] a) D. Etezadi, J. B. t. Warner, H. A. Lashuel, H. Altug, *ACS Sens.* **2018**, *3*, 1109; b) I. Pupeza, M. Huber, M. Trubetskov, W. Schweinberger, S. A. Hussain, C. Hofer, K. Fritsch, M. Poetzlberger, L. Vamos, E. Fill, T. Amotchkina, K. V. Kepesidis, A. Apolonski, N. Karpowicz, V. Pervak, O. Pronin, F. Fleischmann, A. Azzeer, M. Zigman, F. Krausz, *Nature* **2020**, *577*, 52; c) A. G. Brolo, *Nat. Photonics* **2012**, *6*, 709.
- [6] a) J. D. S. Goulden, D. J. Manning, *Nature* **1964**, *203*, 403; b) R. Lu, W.-W. Li, B. Mizaikoff, A. Katzir, Y. Raichlin, G.-P. Sheng, H.-Q. Yu, *Nat. Protoc.* **2016**, *11*, 377.
- [7] a) R. Adato, H. Altug, *Nat. Commun.* **2013**, *4*, 2154; b) O. Limaj, D. Etezadi, N. J. Wittenberg, D. Rodrigo, D. Yoo, S. H. Oh, H. Altug, *Nano Lett.* **2016**, *16*, 1502; c) A. John-Herpin, A. Tittl, H. Altug, *ACS Photonics* **2018**, *5*, 4117; d) D. Rodrigo, A. Tittl, N. Ait-Bouziad, A. John-Herpin, O. Limaj, C. Kelly, D. Yoo, N. J. Wittenberg, S.-H. Oh, H. A. Lashuel, H. Altug, *Nat. Commun.* **2018**, *9*, 2160; e) Y. Jahani, E. R. Arvelo, F. Yesilkoy, K. Koshelev, C. Cianciaruso, M. De Palma, Y. Kivshar, H. Altug, *Nat. Commun.* **2021**, *12*, 3246; f) A. John-Herpin, D. Kavungal, L. von Mücke, H. Altug, *Adv. Mater.* **2021**, *33*, 2006054; g) C. Wu, A. B. Khanikaev, R. Adato, N. Arju, A. A. Yanik, H. Altug, G. Shvets, *Nat. Mater.* **2012**, *11*, 69.
- [8] a) O. L. Daniel Rodrigo, D. Janner, D. Etezadi, F. J. García de Abajo, V. Pruneri, H. Altug, *Science* **2015**, *349*, 165; b) X. Yang, Z. Sun, T. Low, H. Hu, X. Guo, F. J. Garcia de Abajo, P. Avouris, Q. Dai, *Adv. Mater.* **2018**, *30*, 1704896.
- [9] a) I. H. Lee, D. Yoo, P. Avouris, T. Low, S. H. Oh, *Nat. Nanotechnol.* **2019**, *14*, 313; b) H. Hu, X. Yang, F. Zhai, D. Hu, R. Liu, K. Liu, Z. Sun, Q. Dai, *Nat. Commun.* **2016**, *7*, 12334; c) X. Yang, F. Zhai, H. Hu, D. Hu, R. Liu, S. Zhang, M. Sun, Z. Sun, J. Chen, Q. Dai, *Adv. Mater.* **2016**, *28*, 2931; d) H. Hu, X. Yang, X. Guo, K. Khaliji, S. R. Biswas, F. J. Garcia de Abajo, T. Low, Z. Sun, Q. Dai, *Nat. Commun.* **2019**, *10*, 1131.
- [10] a) Y. Hu, Á. I. López-Lorente, B. Mizaikoff, *ACS Photonics* **2018**, *5*, 2160; b) B. Zheng, X. Yang, J. Li, C.-F. Shi, Z.-L. Wang, X.-H. Xia, *Anal. Chem.* **2018**, *90*, 10786.
- [11] S.-H. Oh, H. Altug, X. Jin, T. Low, S. J. Koester, A. P. Ivanov, J. B. Edel, P. Avouris, M. S. Strano, *Nat. Commun.* **2021**, *12*, 3824.
- [12] K. Khaliji, S. R. Biswas, H. Hu, X. Yang, Q. Dai, S.-H. Oh, P. Avouris, T. Low, *Phys. Rev. Appl.* **2020**, *13*, 011002.
- [13] C. J. Russo, L. A. Passmore, *Nat. Methods* **2014**, *11*, 649.
- [14] a) Y. Ohno, K. Maehashi, Y. Yamashiro, K. Matsumoto, *Nano Lett.* **2009**, *9*, 3318; b) Y.-Q. Bie, J. Horng, Z. Shi, L. Ju, Q. Zhou, A. Zettl, D. Yu, F. Wang, *Nat. Commun.* **2015**, *6*, 7593.
- [15] F. Neubrech, C. Huck, K. Weber, A. Pucci, H. Giessen, *Chem. Rev.* **2017**, *117*, 5110.
- [16] a) S. Li, J. Li, Y. Wang, C. Yu, Y. Li, W. Duan, Y. Wang, J. Zhang, *Nat. Electron.* **2021**, *4*, 254; b) A. Ahmadian Yazdi, J. Xu, V. Berry, *ACS Nano* **2021**, *15*, 6998; c) X. Jia, M. Hu, K. Soundarapandian, X. Yu, Z. Liu, Z. Chen, A. Narita, K. Müllen, F. H. L. Koppens, J. Jiang, K.-J. Tielrooij, M. Bonn, H. I. Wang, *Nano Lett.* **2019**, *19*, 9029.
- [17] a) J. Atzrodt, V. Derdau, W. J. Kerr, M. Reid, *Angew. Chem., Int. Ed.* **2018**, *57*, 1758; b) G. R. Masson, J. E. Burke, N. G. Ahn, G. S. Anand, C. Borchers, S. Brier, G. M. Bou-Assaf, J. R. Engen, S. W. Englander, J. Faber, R. Garlish, P. R. Griffin, M. L. Gross, M. Guttman, Y. Hamuro, A. J. R. Heck, D. Houde, R. E. Iacob, T. J. D. Jørgensen, I. A. Kaltashov, J. P. Klinman, L. Konermann, P. Man, L. Mayne, B. D. Pascal, D. Reichmann, M. Skehel, J. Snijder, T. S. Strutzenberg, E. S. Underbakke, et al., *Nat. Methods* **2019**, *16*, 595; c) Y. Loh Yong, K. Nagao, J. Hoover Andrew, D. Hesk, R. Rivera Nelo, L. Colletti Steven, W. Davies Ian, W. C. MacMillan David, *Science* **2017**, *358*, 1182.
- [18] L. Konermann, J. Pan, Y.-H. Liu, *Chem. Soc. Rev.* **2011**, *40*, 1224.
- [19] J. J. Weiss, *Nature* **1964**, *202*, 83.
- [20] a) M. A. Ordal, L. L. Long, R. J. Bell, S. E. Bell, R. R. Bell, R. W. Alexander, C. A. Ward, *Appl. Opt.* **1983**, *22*, 1099; b) D. Rodrigo, A. Tittl, O. Limaj, F. J. García de Abajo, V. Pruneri, H. Altug, *Light: Sci. Appl.* **2017**, *6*, e16277.